

The Relationship Between Microstructure and Fracture Toughness for Fibrous Materials for Diesel Particulate Filters

Tim Gordon

GEO2 Technologies Inc., Woburn, Massachusetts 01801

Amit Shyam^{*,†} and Edgar Lara-Curzio^{**}

Oak Ridge National Laboratory, Materials Science and Technology Division, Oak Ridge, Tennessee 37831

The Mode I fracture toughness of fibrous SiC and mullite materials with 60%–70% porosity was determined under ambient conditions using the double-torsion test method. The fracture toughness values obtained were 0.27 and 0.34 MPa·m^{1/2} for fibrous SiC and mullite, respectively. These fibrous ceramics exhibit greater fracture resistance than porous monolithic ceramics with similar levels of porosity. A higher degree of cross-linking between the fibers led to further improvement in the fracture characteristics of the fibrous material. The differences in fracture behavior can be explained by the microstructural differences between these two classes of materials. The combination of high porosity and high fracture toughness for fibrous materials makes them ideal candidates for applications in diesel particulate filtration.

I. Introduction

EMISSION control devices are being used by the trucking industry to meet increasingly stringent regulations. In the United States, emissions from diesel engines produced after January 1, 2007 were required to reduce nitrogen oxides (NO_x) by 50% and particulate matter (PM) emissions by 90%. By 2010 it will be necessary to reduce nitrogen oxide (NO_x) emissions by an additional 83% from 2007 levels.

To reduce complexity and costs it would be desirable to utilize a single substrate capable of PM filtration, selective catalytic reduction, lean NO_x trapping, and hydrocarbon oxidation to achieve the mandated emission reductions. Compared with substrates for a single-function (e.g., diesel particulate filtration), such multifunctional substrates must have greater porosity to accommodate the incorporation of increased loadings of wash-coat and catalysts. However, even for single-function substrates, such as diesel particulate filters (DPFs), there are compelling reasons for optimizing such microstructural features as the distribution of pore sizes and pore shapes, because these parameters determine the filtration performance and backpressure.

The filtration performance and structural integrity of most filter materials have competing microstructural requirements. For example, increasing porosity has the beneficial effect of reducing backpressure with resulting increases in engine efficiency; however, in the case of ceramic substrates, high porosity tends to reduce the substrate's resistance to fracture. DPFs operate under severe conditions. These include temperature gradients, engine

vibrations and exposure to the diesel engine exhaust gas stream. Given the challenging thermomechanical environment under which DPFs operate, there is considerable interest in optimizing the physical and mechanical properties of existing DPF materials^{1–4} and in developing new materials^{5–8} with engineered microstructures that exhibit superior mechanical properties. Ceramic fibrous materials are a natural choice to consider for DPFs because they are inherently tougher than their porous monolithic counterparts, which makes it possible to design DPFs with high porosity and high fracture toughness.

In this paper we report on the fracture behavior of two new, highly porous, fibrous ceramic materials with a unique Cross-Linked Microstructure (CLM[™])^{9,10} and compare the properties of these materials with those of porous monolithic ceramic materials that are currently being used to manufacture DPFs.

II. Experimental Procedure

The mechanical properties of ceramic DPF substrate materials have been determined by evaluating sections of the cellular structure containing multiple channels,¹¹ or by evaluating thin plates obtained from the walls of the cellular structure.¹² In this study, the properties of fibrous SiC and mullite materials are determined following the latter approach, which provides a means for direct comparison of the intrinsic material properties of materials and to assess the effects of microstructural differences.¹²

(1) Sample Preparation

The materials used for this investigation were fabricated by GEO2 Technologies Inc. (Woburn, MA). The ceramic honeycomb structures were extruded from ceramic paste by preparing mixtures with the following typical batch compositions (in wt%): GEO2 SiC starting mixture contained chopped carbon fibers 17.9%, colloidal silica (50% solution in water) 59.7%, hydroxypropyl methylcellulose (HPMC) binder 10.0% and deionized water 12.4%; GEO2 mullite starting mixture contained mullite fibers 22.1%, bentonite strengthener 2.2%, HPMC 10.3%, propylene glycol plasticizer 1.1%, polymethyl methacrylate (PMMA) pore former 36.8% and water 27.5%. The starting fibers were chopped with a minimum diameter of 3 μm and lengths in the range 5–50 mm. A high-shear sigma blade mixer was used for approximately 60 min to mix the constituents to form a ceramic paste. The pastes were subsequently deaired before forming into a billet and then extruded in a hydraulic ram extruder at a rate of 10 m/min into a square honeycomb bar with dimensions of 36 mm. The extrusion parameters were adjusted in real time to account for the variation in the rheological parameters for each batch of paste. The extruded part was dried and sintered in a radio-frequency oven to obtain a final cell density of 300 cells/in.² and 0.305 mm cell wall thickness. A detailed description of the processes and materials for the fabrication of these materials can be found elsewhere.^{9,10} The phases present in

A. Bandyopadhyay—contributing editor

Manuscript No. 26626. Received 30 July 2009; approved 2 November 2009.

The research at the Oak Ridge National Laboratory's High Temperature Materials Laboratory was sponsored by the U. S. Department of Energy, Office of Energy Efficiency and Renewable Energy, Vehicle Technologies Program.

^{*}Member, The American Ceramic Society.

[†]Author to whom correspondence should be addressed. e-mail: shyama@ornl.gov

^{**}Fellow, The American Ceramic Society.

these materials, as determined by X-ray diffraction, are listed in Table I.

Test specimens for determination of fracture properties were obtained from 144 mm diameter \times 152 mm length multichannel DPFs by first excising a single-channel thick section and then dry grinding this section to produce a single wall test specimen of dimensions 40 mm \times 20 mm \times 0.250 mm. Figure 1 represents a schematic depiction of a double-torsion specimen prepared from a wall of a ceramic honeycomb. Length and width dimensions in a double-torsion test specimen typically varied by $<1\%$ both within a single specimen and between specimens, and thickness variation—more challenging to maintain due to the delicacy of the test specimen—was limited to 5%.

A 0.300 mm thick wafering blade was used to produce an approximately 0.350 mm wide and 12 mm long notch to prepare double torsion test specimens. As depicted in Fig. 1, all specimens were prepared such that the notch (and the crack emanating from it) runs parallel to the extrusion direction. This orientation is known to be the “weak” orientation¹² in the extrusion plane. Specially designed vacuum chucks were used to hold the specimens during the machining operations. Details of the specimen grinding and notching procedure have been reported elsewhere.¹²

(2) Microstructural Characterization

The porosity of the fibrous materials was calculated using three techniques: (a) mercury intrusion porosimetry (MIP, Micromeritics, Norcross, GA, AutoPore IV 9500 v1.07), (b) image analysis of ceramographically prepared specimens, and (c) ratio of specimen density to bulk density.

For image analysis, one-half of one double-torsion test specimen from each material was ceramographically prepared after fracture testing and analyzed in a scanning electron microscope. The long side of the double-torsion specimen (40 mm) was examined in all cases for consistency in observation with respect to the extrusion direction in the filter. The prepared specimens were coated with carbon before observation. Twenty scanning electron microscopic (SEM) images were acquired for every specimen and subsequently adjusted for contrast, thresholded and then reduced to a binary representation. The average porosity was calculated as the fraction of black pixels in the twenty images.

According to the third technique the porosity of test specimens was determined by the ratio of density of the test specimen and the bulk density according to the following relationship:

$$\% \text{ porosity} = \frac{\text{specimen density}}{\text{bulk density}} \times 100\% \quad (1)$$

The density of test specimens was determined by the ratio of their mass to the volume defined by the envelope dimensions of the parallelepiped specimen. The assumed bulk densities for SiC and mullite were: 3.24 and 3.16 g/cm³, respectively. Because these materials contained more than one phase (Table I) and there is uncertainty about the exact volume fraction of the phases that uncertainty will propagate through to the determination of porosity when using Eq. (1).

Fiber diameter distributions were obtained for the SiC and mullite substrate materials by measuring the diameter of 200 fibers in ceramographically prepared specimens. A Hitachi S-4800 UHR FEG-SEM (Pleasanton, CA) was used to analyze the microstructures of the materials studied in this investigation. A

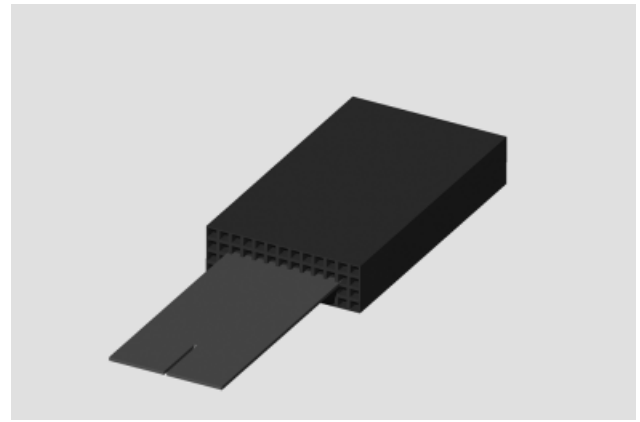


Fig. 1. Schematic depiction of the location of a double-torsion fracture toughness test specimen that was excised from the ceramic honeycomb structure. The length of the specimen is parallel to the extrusion direction.

Hitachi S-3400 Environmental-SEM was used to acquire micrographs of the fracture surfaces of double torsion test specimens.

(3) Fracture Toughness Testing

Standardized testing methodologies have recently been developed for evaluating the flexural strength of honeycomb structures.¹³ Such standardized test methods are necessary to allow for the direct comparison of the mechanical properties of honeycomb structures given the large number of variables associated with their geometry and the effect of these variables on mechanical properties, such as strength. Another approach to determine the mechanical properties of honeycomb structures consists of preparing test specimens obtained from the walls of the cellular structure channels. This approach has been shown to be an effective procedure to obtain elastic properties using resonant ultrasound spectroscopy and fracture toughness using the double-torsion test method.¹² The latter test technique has the advantage that there is no need to grip the test specimen, because gripping fragile test specimens, such as those under consideration for the fabrication of DPFs, constitutes a significant challenge. Another feature of the double-torsion test method is that the stress intensity factor is independent of crack length for a range of crack lengths. This feature of the test method provides an advantage because there is no need to obtain direct measurements of crack length, which are difficult to obtain for porous materials. A review of the advantages and disadvantages of the double-torsion testing methodology compared with other methodologies can be found elsewhere.¹⁴

The methodology for the fracture toughness tests has been described in detail elsewhere.¹² In summary, notched, test specimens were placed on an alumina articulated double torsion fixture. Tests were conducted in the ambient environment (between 24° and 27°C with 20%–35% relative humidity) using an MTS 808 electromechanical testing machine (MTS®, Eden Prairie, MN) equipped with a miniature 2.45 N load cell (Sensotec®, Model 31; Honeywell Sensotec, Columbus, OH). Specimens were precracked by loading test specimens at a constant crosshead displacement rate of 1 μ m/s until deviation from linearity in the load/displacement curve and/or several small drops in load were noted. The precrack load value was recorded and the test specimen was unloaded. The crosshead displacement rate

Table I. Composition of the Fibrous Materials Investigated

Material	Form	Chemical composition (approx. wt%)	Manufacturer
SiC	Fibrous	α -SiC ($>90\%$); Si ($<5\%$); amorphous silica phase ($<5\%$)	GEO2
Mullite	Fibrous	$\text{Al}_6\text{Si}_2\text{O}_{13}$ —Mullite (72%); SiO_2 ($<5\%$); amorphous silica phase ($<25\%$)	GEO2

was increased to 10 $\mu\text{m/s}$ and the test specimen was loaded monotonically until fracture occurred. The maximum load, P_{IC} , was recorded and subsequently used to determine the fracture toughness of the material. Tests in which the crack intersected the long (40 mm) side of the specimen were excluded from the analysis; it is assumed that misalignment of the fixture, poor specimen preparation or other nonstandard conditions are responsible for such results, for in the absence of such conditions, the crack is expected to propagate along the length of the specimen and intersect the short (20 mm) side. Fewer than 10% of the tests conducted in this investigation were deemed invalid based on this criterion.

III. Results and Discussion

(1) Microstructural Characterization

The fibrous structure of the two GEO2 materials is apparent in the SEM micrographs of Figs. 2(a) and (b). The extrusion direction is parallel to the horizontal orientation of these images. Higher magnification SEM images are presented in Figs. 3(a) and (b). It was found that the fibers have a circular/elliptical cross-section and that they tend to agglomerate resulting in irregular shapes as observed in Fig. 3. The SiC fibers (Figs. 2(a) and 3(a)) tend to be aligned parallel to the extrusion direction in contrast to the mullite fibers (Figs. 2(b) and 3(b)), which tend to interlock resulting in a more random fiber architecture. This is attributed to differences in the raw materials and fabrication processes. In fabricating GEO2 SiC the extruded wet material contains self-lubricating carbon fiber precursors, which when forced sequentially through dies are able to align along the extrusion direction better than the mullite fibers that are used as the precursors in the mullite product. The extruded mullite

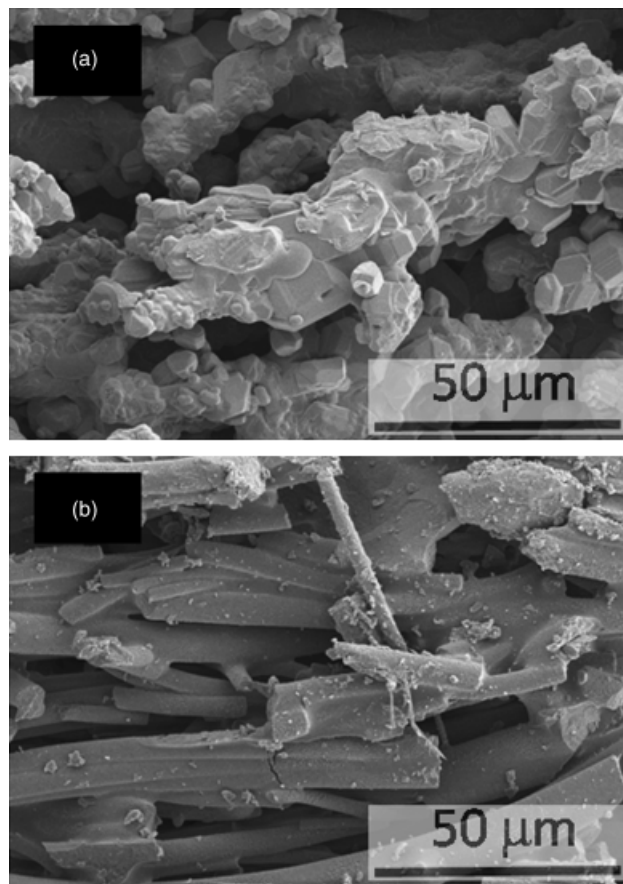


Fig. 3. Higher magnification scanning electron microscopic images of (a) GEO2 fibrous SiC, (b) GEO2 fibrous mullite. Note the differences in fiber morphology showing the differences in the two fibrous materials.

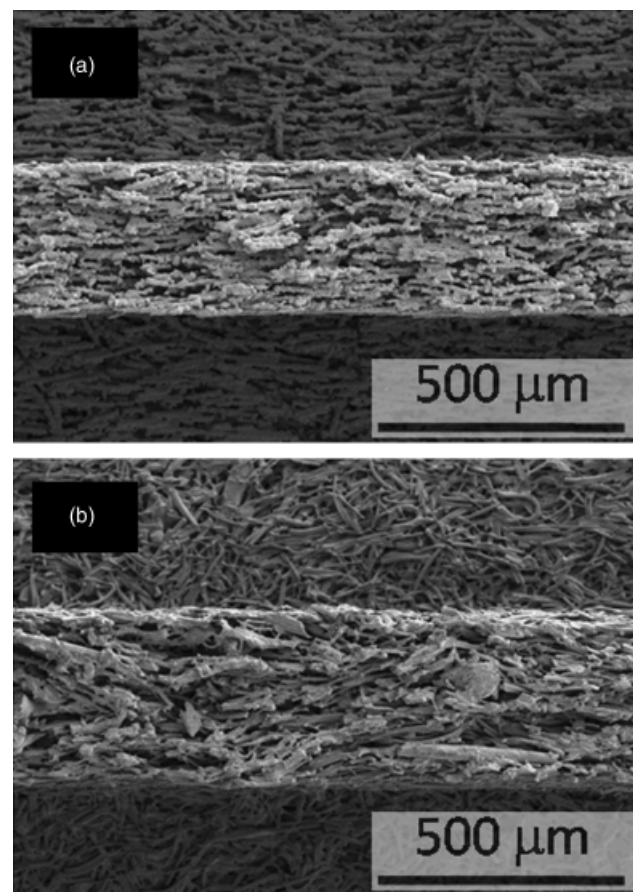


Fig. 2. Scanning electron micrographs of: (a) GEO2 fibrous SiC, (b) GEO2 fibrous mullite. The extrusion direction is parallel to horizontal orientation in these images.

material, conversely has a more random fiber distribution with a higher degree of fiber interlocking.

The distributions of fiber diameters for the SiC and mullite fibrous materials are plotted in Fig. 4. For each material, the distribution is based on measurement of 200 individual fibers imaged in the ceramographically prepared specimens using a scanning electron microscope. The average fiber diameter value (± 1 standard deviation) for SiC and mullite substrates is 10.41 ± 3.79 and 6.48 ± 2.59 μm , respectively.

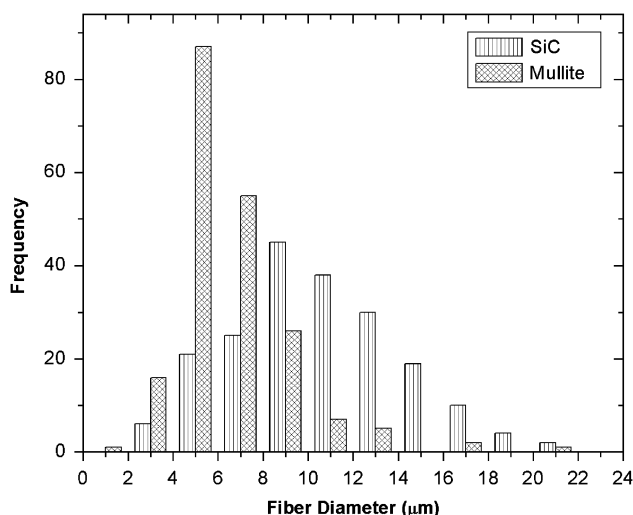


Fig. 4. The distribution of fiber diameters for the SiC and mullite fibrous DPF substrates. A total of 200 fibers were measured for each material.

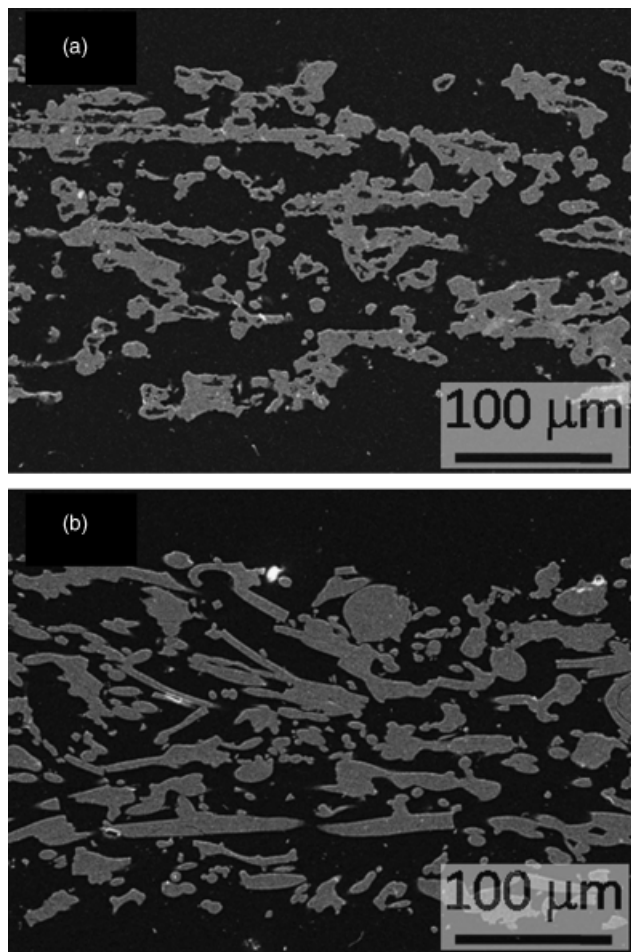


Fig. 5. Scanning electron micrographs of ceramographically prepared test specimens (a) GEO2 fibrous SiC (porosity = 68.1%); (b) GEO2 fibrous mullite (porosity = 62.4%).

The SEM images in Fig. 5 are typical of those that were obtained from the cross section of ceramographically prepared specimens of the two fibrous materials. In Fig. 5, the extrusion direction is parallel to the horizontal orientation in the image. Some α -SiC fibers in Fig. 5(a) have an unreacted carbon core while others appear to be hollow, perhaps as a result of the oxidation of the carbon core. These images are processed according to the technique described earlier in this paper to estimate the porosity of the materials. The porosity data calculated from the analysis of these images are listed in Table II. It was found that the porosity values from image analysis are similar to the values obtained from MIP. Also listed in Table II are porosity values calculated from the relative density measurement according to Eq. (1). The porosity values obtained from relative density measurements were found to be higher than those obtained using the other two techniques. The main reasons for the discrepancy are assumptions about the value of the bulk density and uncertainty about the purity of the material. Variability in the

Table II. Summary of Average Porosity Values (\pm Standard Deviation) for the Fibrous Substrates from the Three Different Measurement Techniques

Material	Porosity measurements (%)		
	MIP	Image analysis	Relative density
Mullite-fiber	62 \pm 3.7	63 \pm 2.6	70 \pm 2.5
SiC-fiber	67 \pm 2.0	68 \pm 2.5	73 \pm 1.3

MIP, mercury intrusion porosimetry.

thickness of the test specimens is also expected to contribute to the discrepancy.

(2) Fracture Toughness

The critical value of stress intensity factor for fast fracture is given by the Mode I fracture toughness, K_{IC} . Assuming plane stress conditions, K_{IC} in the double-torsion testing geometry is given by

$$K_{IC} = P_{IC} S_m \sqrt{\frac{3(1+\nu)}{S t^4 \psi}} \quad (2)$$

where P_{IC} is the failure load, ν is Poisson's ratio, S is the width of the specimen, S_m is the moment arm applied on the specimen, t is the specimen thickness and ψ is a finite beam thickness correction factor.¹⁵ In this analysis Poisson's ratio of the fibrous materials was assumed equal to 0.24.

The fracture toughness of at least five specimens for each of the two fibrous materials was determined and the average values are presented as a function of the average porosity of the substrate in Fig. 6. The average and standard deviation of porosity values represented in Fig. 6 were based on the calculated porosity values of the tested double-torsion specimens. The porosity values were calculated by determining the bulk density of one specimen according to Eq. (1). The specimen density of this specimen was known from a mass per unit volume calculation and the porosity of the specimen from the image analysis determination. The bulk density was then utilized to calculate the porosity of the individual double-torsion test specimens (before notching) based on the density of the individual specimens. Included in Fig. 6 are data obtained from the evaluation of commercially available porous monolithic SiC and cordierite DPF substrate materials. Cordierite substrates were made by Corning Inc. (DuraTrap[®], Corning, NY), while SiC substrates were manufactured by NGKz (Nagoya, Japan). Table III lists other characteristics of these materials. In addition, unpublished data for similar cordierite formulations as in the current work are plotted (four data points connected with a trendline) (A. Shyam *et al.*, unpublished results) in Fig. 6. Considering other differences between the cordierite formulations, there is good agreement between the fracture toughness values in the previous data (cordierite—porous monolithic 2 contains information from different manufactures with substrates containing catalytic wash-coating, soot, etc.) and the fracture toughness of the current cordierite—porous monolithic 1. The specimen preparation, microstructural and fracture mechanical characterization procedures described above were applied to the two materials.

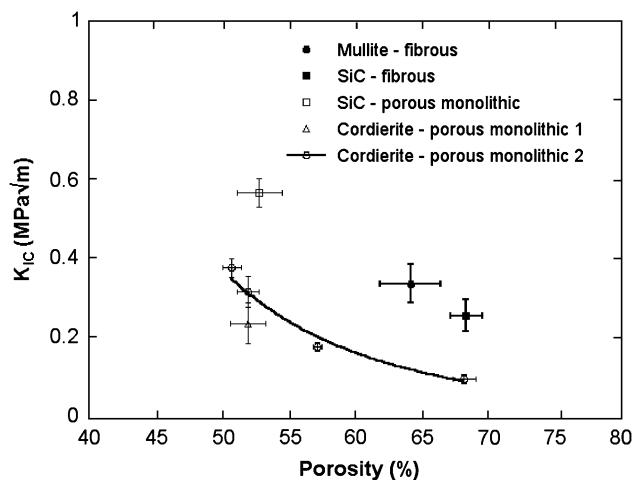


Fig. 6. Fracture toughness (± 1 standard deviation) as a function of porosity (± 1 standard deviation) for porous monolithic and fibrous materials. The four data points connected with the trendline are from an earlier study (A. Shyam *et al.*, unpublished results).

Table III. Description of the Porous Monolithic DPF Substrates

Material	Honeycomb structure	Manufacturer
Cordierite	200 cells/in. ² 0.305 mm cell wall thickness	Corning Inc.
SiC	200 cells/in. ² 0.305 mm cell wall thickness	NGK Insulators Limited

DPF, diesel particulate filters.

SEM images of the microstructure of the porous monolithic SiC and cordierite materials are shown in Figs. 7(a)–(c) and (b)–(d), respectively. The SiC grains are on average larger than the cordierite grains and more uniform in shape. Images of the cross-section for the porous monolithic substrate materials are also included in Figs. 7(e)–(f). The higher aspect ratio of the microstructural constituents in the fibrous materials, i.e. fibers compared with cordierite and SiC domains is evident when comparing Figs. 7(e)–(f) with Fig. 5.

T-tests confirmed ($p = 0.403$) that the fracture toughness of GEO2 fibrous SiC ($0.265 \pm 0.042 \text{ MPa} \cdot \text{m}^{1/2}$ at 68.1% porosity) is equivalent to that of porous monolithic cordierite ($0.242 \pm 0.051 \text{ MPa} \cdot \text{m}^{1/2}$ at 51.5% porosity). Furthermore, it was found that at $0.340 \pm 0.048 \text{ MPa} \cdot \text{m}^{1/2}$ (62.7% porosity), GEO2's fibrous mullite material possesses significantly *greater* ($p = 0.014$) fracture toughness than porous monolithic cordierite with an equivalent level of porosity.

Green and colleagues^{16,17} developed a micromechanical model to relate the fracture properties of fibrous ceramic bodies to their microstructure and the properties of their fibrous constituents. They found that the fracture toughness of the fibrous structure depends on the density of the body with respect to the density of the fibers, the degree of fiber orientation, fiber strength and fiber diameter. According to this model the expression for fracture toughness of bulk specimens in the weak direction (K_{c3}) relative to the properties of the fiber is given by the following equation:

$$K_{c3} \cong 1.67 \left[\frac{\rho}{\rho_f} \left(\frac{E_3}{E_3 + 2E_2} \right) \right]^{3/4} \sigma_{fb} r^{1/2} \quad (3)$$

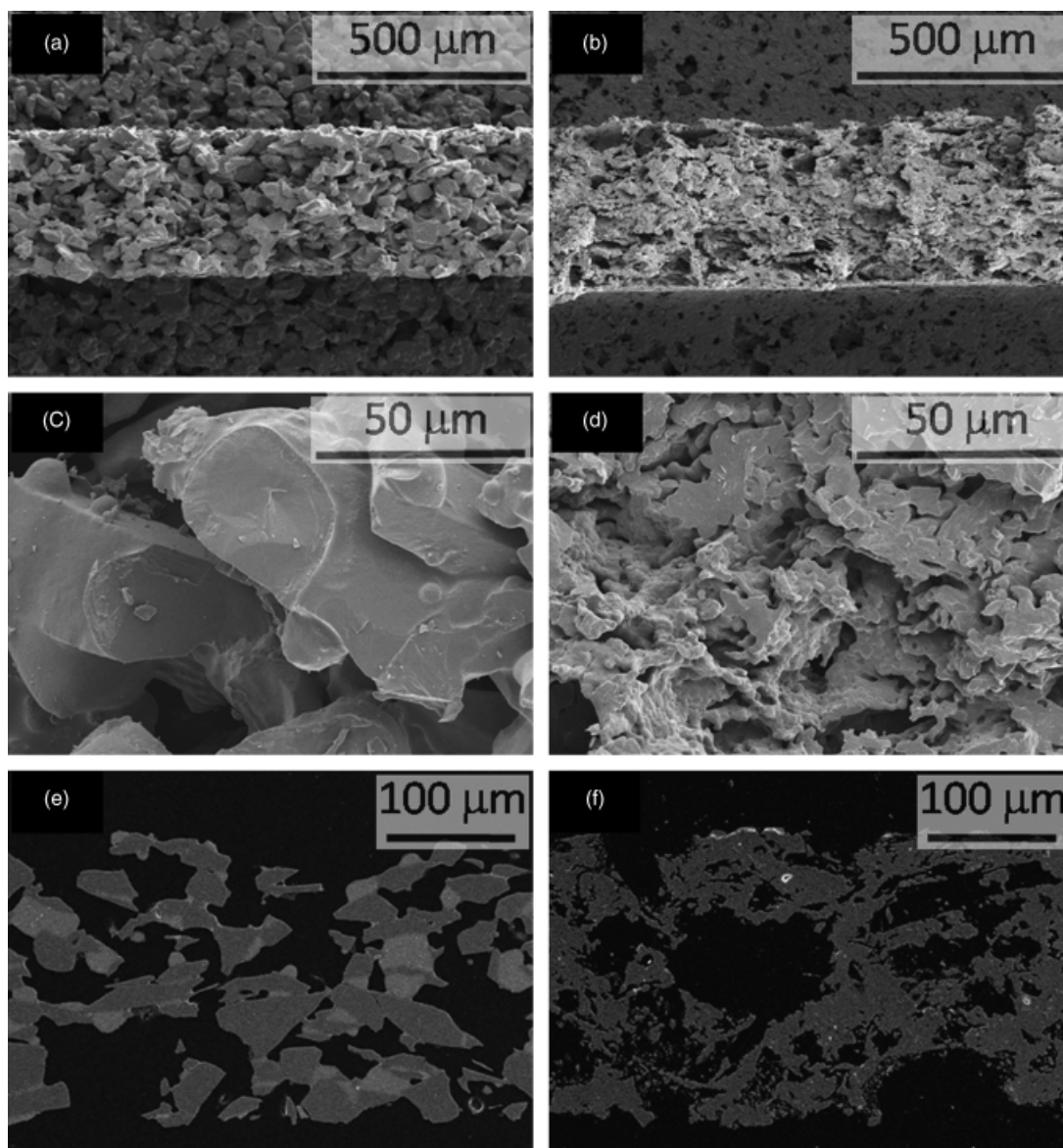


Fig. 7. Scanning electron microscopic (SEM) images of the porous monolithic materials: (a) SiC, (b) cordierite, (c) higher magnification SiC, (d) higher magnification cordierite. SEM images of ceramographically prepared test specimens with porosities typical for each material, (e) porous monolithic SiC (porosity = 53.8%), (f) porous monolithic cordierite (porosity = 52.0%).

where r is the radius of the fiber, σ_{fb} is the fiber strength, E_2 and E_3 are Young's moduli in the strong and weak directions of the bulk material, ρ is the density of the fibrous material and ρ_f the theoretical density of the fiber. This equation can be rewritten assuming the material is elastically isotropic ($E_3 = E_2$) in the following manner

$$K_{c3} \cong 0.73 \left[\frac{\rho}{\rho_f} \right]^{3/4} \sigma_{fb} r^{1/2} \quad (4)$$

For the case of $E_3 = 0.5E_2$, the proportionality constant changes from 0.73 to 0.50. Equation (4) can be utilized to understand the effect of different parameters on the fracture behavior of fibrous substrates. Specifically, the fracture resistance of the material can be enhanced by: (a) increasing its density (ρ/ρ_f or by decreasing its porosity); (b) increasing the strength of the fibers; and (c) increasing the fiber diameter, although for ceramic fibers increases in the diameter can be accompanied by decreases in fiber tensile strength due to strength size effects.

Substituting the fracture toughness values, the porosity and the average fiber radius into Eq. (4) leads to estimates of fiber strength of 209 and 361 MPa for SiC and mullite fibers, respectively. One possible reason for the relatively low-strength value of the SiC fibers is that some of the fibers have an unreacted core of carbon as shown in Fig. 5(a). Okada *et al.*¹⁸ reported on the synthesis of SiC fibers by reacting activated carbon fibers with gaseous silicon monoxide. The authors found that the resulting fibers had an unreacted carbon core, which could be removed by heating the fiber in air, resulting in a hollow SiC fiber. They also found that the strength of the fibers could be increased from 300 to 1000 MPa after the fibers were heat treated in nitrogen at 1600°C. Using a similar process Kowbel *et al.*¹⁹ converted T-300 carbon fibers into SiC fibers and reported tensile strengths of 2.1 GPa for 55% converted fibers.

Analysis of the microstructure of the fibrous SiC material (Fig. 8) revealed that this material exhibits a lower degree of cross-linking compared with the fibrous mullite material. Figures 8(a) and (b) reveal the microstructure of the fibrous material in the extrusion plane. Green and Lange¹⁶ had suggested that σ_{fb} not only reflects the actual tensile strength of the fibers but also how well they are bonded to one another. Ortiz-Lango and White²⁰ demonstrated that the fracture behavior of fibrous thermal insulator materials is related to the bulk microstructures, the properties of the fibers, and the fiber-to-fiber bond chemistry. In the analysis of failure processes in fibrous materials it is, therefore, important to consider that crack growth occurs both by fiber breakage and breakage of the bonds between the fibers. Therefore, a greater degree of cross-linking is expected to promote greater fracture resistance as evidenced by the micrograph in Fig. 8(b), which illustrates the tortuous path of the crack. In summary, fiber-based DPF substrate materials not only demonstrate improved fracture resistance compared with their porous monolithic counterparts but their resistance to fracture can be enhanced by improving the degree of cross-linking between the fibers.

(3) Other Properties of Relevance for DPF applications

High fracture toughness (or strength) is only one of the desirable attributes for a durable and high thermal shock resistant DPF substrate material. The simplest expression for a thermal shock parameter (R_S) is the following²¹:

$$R_S = \frac{\sigma_f}{E\alpha} \quad (5)$$

where, σ_f represents the failure strength, E is the modulus and α is the coefficient of thermal expansion. The above expression ignores other parameters, such as thermal conductivity, which affect the thermal shock resistance and are also affected by porosity of the substrate. Equation (5) implies that design of a

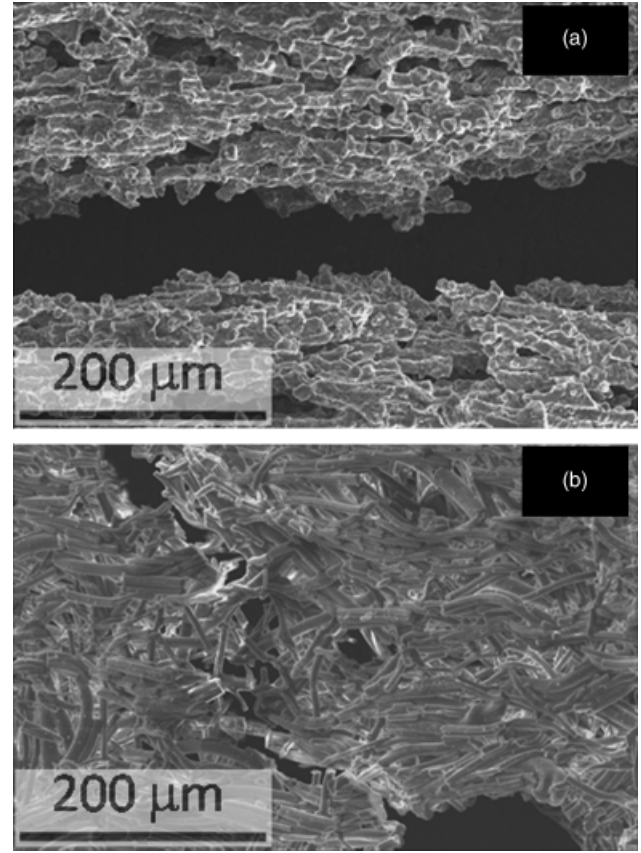


Fig. 8. Scanning electron microscopic images of the two broken halves of each fracture toughness specimen reveal the much greater degree of order and extrusion direction alignment with (a) GEO2 fibrous SiC and the randomness of (b) GEO2 fibrous mullite (crack extends from notch in lower right to upper left corner).

high thermal shock resistant material would require a high strength (or fracture toughness) material but with low elastic modulus. Indeed, the higher level of overall porosity in fibrous substrates has been shown to keep the elastic moduli of these materials at comparable or lower values compared with their porous monolithic counterparts.¹⁰

For DPF applications, the functional requirements of the substrate materials include low-pressure drop and high filtration efficiency. The effect of substrate porosity on filtration efficiency and pressure drop has been discussed by other researchers.²²⁻²⁵ The pressure drop performance and filtration efficiency is related to total porosity, pore shape and size distribution and microstructure. It has been shown that the crosslinked microstructure of fibrous substrates helps increase their filtration efficiency with lower pressure drop compared with porous monolithic substrates.¹⁰ Liu *et al.*¹⁰ attributed the improved filtration performance to the pore size distribution and higher degree of connectivity in the fibrous microstructure.

IV. Conclusions

The fracture toughness of two fibrous materials was determined using the double-torsion test method. The fracture toughness of fibrous SiC with 68% porosity was $0.27 \text{ MPa} \cdot \text{m}^{1/2}$ while that of fibrous mullite with 63% porosity was $0.34 \text{ MPa} \cdot \text{m}^{1/2}$. It was found that for a given value of porosity, these fibrous materials are tougher than porous monolithic ceramics. The role of the microstructure on the fracture behavior of these materials was analyzed and the results were found to be consistent with the micromechanical model of Green for fibrous ceramics.

Acknowledgments

The authors thank Randy Parten of ORNL for his assistance in the preparation of test specimens and Larry Walker (ORNL) for his assistance with the operation of the SEM. The authors also thank Hsin Wang (ORNL) and Michael Lance (ORNL) for reviewing the manuscript.

References

- ¹Y. Hiratsuka, M. Ishihara, M. Tanaka, J. Suzuki, and N. Takagi, "The Latest Technology of Controlling Micro-Pore in Cordierite Diesel Particulate Filter for DPNR System"; SAE Paper No. 2004-01-2028, 2004.
- ²C. Barataud, S. Bardon, B. Bouteiller, V. Gleize, A. Charlet, and P. Higelin, "Diesel Particulate Filter Optimization"; SAE Paper No. 2003-01-0376, 2003.
- ³I. Melscoet-Chauvel, C. Remy, and T. Tao, "High Porosity Cordierite Filter Development for NO_x/PM Reduction Developments," *Dev. Adv. Ceram. Compos.: Ceram. Eng. Sci. Proc.*, **26** [8] 11–9 (2005).
- ⁴S. Miwa, F. Abe, T. Hamanaka, T. Yamada, and Y. Miyairi, "Diesel Particulate Filters Made of Newly Developed SiC"; SAE Paper No. 2001-01-0192, 2001.
- ⁵N. D. Vlachos and A. G. Konstandopoulos, "Digital Materials for DPF Development"; SAE Paper No. 2006-01-0260, 2006.
- ⁶J. Tulliani, L. Montanaro, T. J. Bell, and M. V. Swain, "Semiclosed-Cell Multilite Foams: Preparation and Macro- and Micromechanical Characterization," *J. Am. Ceram. Soc.*, **82** [4] 961–8 (1999).
- ⁷W. A. Cutler and G. A. Merkel, "A New High Temperature Ceramic Material for Diesel Particulate Filter Applications"; SAE Paper No. 2000-01-2844, 2000.
- ⁸A. J. Pyzik and C. G. Li, "New Design of a Ceramic Filter for Diesel Emission Control Applications," *Int. J. Appl. Ceram. Technol.*, **2** [6] 440–51 (2005).
- ⁹B. Zuberi, J. J. Liu, S. C. Pillai, J. G. Weinstein, A. G. Konstandopoulos, S. Lorentzou, and C. Pagoura, "Advanced High Porosity Ceramic Honeycomb Wall Flow Filters"; SAE Paper No. 2008-01-0623, 2008.
- ¹⁰J. J. Liu, R. A. Dahl, T. Gordon, and B. Zuberi, "Use of Ceramic Microfibers to Generate a High Porosity Cross-Linked Microstructure in Extruded Honeycombs," *Adv. Bioceram. Porous Ceram. II: Ceram. Eng. Sci. Proc.*, **30** [6] 267–80 (2009).
- ¹¹J. E. Webb, S. Widjaja, and J. D. Helfinstine, "Strength Size Effects in Cellular Ceramic Structures," *Mech. Prop. Perform. Eng. Ceram. II: Ceram. Eng. Sci. Proc.*, **27** [2] 521–32 (2008).
- ¹²A. Shyam, E. Lara-Curzio, T. R. Watkins, and R. J. Parten, "Mechanical Characterization of Diesel Particulate Filter Substrates," *J. Am. Ceram. Soc.*, **91** [6] 1995–2001 (2008).
- ¹³ASTM International. *Standard Test Method for Flexural Strength of Advanced Ceramics with Engineered Porosity (Honeycomb Cellular Channels) at Ambient Temperatures. ASTM Standard C1674-08*. ASTM International, West Conshohocken, PA, 1998.
- ¹⁴A. Shyam and E. Lara-Curzio, "The Double-Torsion Testing Technique for Determination of Fracture Toughness and Slow Crack Growth Behavior of Materials: A Review," *J. Mater. Sci.*, **41**, 4093–104 (2006).
- ¹⁵E. R. Fuller Jr., "An Evaluation of Double-Torsion Testing—Analysis"; pp. 3–18 in *Fracture Mechanics Applied to Brittle Materials—ASTM STP 678*, Edited by S. W. Freiman. American Society for Testing and Materials, Philadelphia, PA, 1979.
- ¹⁶D. J. Green and F. F. Lange, "Micromechanical Model for Fibrous Ceramic Bodies," *J. Am. Ceram. Soc.*, **65** [3] 138–40 (1982).
- ¹⁷D. J. Green, "Fracture Toughness/Young's Modulus Correlation for Low-Density Fibrous Silica Bodies," *J. Am. Ceram. Soc.*, **66** [4] 288–92 (1983).
- ¹⁸K. Okada, H. Kato, R. Kubo, and N. Nakajima, "Preparation of Silicon Carbide Fiber from Activated Carbon Fiber and Gaseous Silicon Monoxide," *Ceram. Eng. Sci. Proc.*, **16** [4] 45–54 (1995).
- ¹⁹W. Kowbel, J. C. Withers, R. O. Loutfy, C. Bruce, and C. Kyriacou, "Silicon Carbide Fibers and Composites from Graphitic Precursors for Fusion Energy Applications," *J. Nucl. Mater.*, **219**, 15–25 (1995).
- ²⁰C. R. Ortiz-Lango and K. W. White, "Elevated-Temperature Fracture Characterization of Advanced Fibrous Ceramic Thermal Insulators," *J. Am. Ceram. Soc.*, **77** [10] 2703–11 (1994).
- ²¹D. Munz and T. Fett, *Ceramics: Mechanical Properties, Failure Behaviour, Materials Selection*. Springer, New York, NY, 1999.
- ²²A. G. Konstandopoulos and J. H. Johnson, "Wall-Flow Diesel Particulate Filters—their Pressure Drop and Collection Efficiency"; pp. 625–47, SAE Trans. 98 sec. 3 (J. Engines) Paper No. 890405, 1989.
- ²³A. G. Konstandopoulos, E. Kladopoulou, and E. Skaperdas, "Transient Filtration of Soot Particles in Ceramic Filters," *J. Aerosol Sci.*, **31** [Suppl. 1] S208–9 (2000).
- ²⁴M. S. Nikitidis, T. Manikas, D. Zarvalis, N. Divinis, C. Altiparmakis, and A. G. Konstandopoulos, "Collection Efficiency of Various Filter Media in Diesel Exhaust"; ICE 2001, 5th International Conference On Internal Combustion Engine, September 23–28, 2001, Capri, Italy, SAE_NA Tech. Paper No. 2001-01-065, 2001.
- ²⁵J. Yang, M. Stewart, G. D. Maupin, D. R. Herling, and A. Zelenyuk, "Single Wall Diesel Particulate Filter (DPF) Filtration Efficiency Studies Using Laboratory Generated Particles," *Chem. Eng. Sci.*, **64** [8] 1625–34 (2009). □